Multiscale modeling of fatigue crack propagation in additively manufactured porous biomaterials

Hedayati, R.; Hosseini-Toudeshky, H.; Sadighi, M.; Mohammadi-Aghdam, M.; Zadpoor, A. A.

DOI
10.1016/j.ijfatigue.2018.05.006

Publication date
2018

Document Version
Accepted author manuscript

Published in
International Journal of Fatigue

Multiscale modeling of fatigue crack propagation in additively manufactured porous biomaterials

R. Hedayati, H. Hosseini-Toudeshky, M. Sadighi, M. Mohammadi-Aghdam, A.A. Zadpoor

PII: S0142-1123(18)30177-4
DOI: https://doi.org/10.1016/j.ijfatigue.2018.05.006
Reference: JIJF 4678

To appear in: *International Journal of Fatigue*

Received Date: 12 February 2018
Revised Date: 2 May 2018
Accepted Date: 4 May 2018

Please cite this article as: Hedayati, R., Hosseini-Toudeshky, H., Sadighi, M., Mohammadi-Aghdam, M., Zadpoor, A.A., Multiscale modeling of fatigue crack propagation in additively manufactured porous biomaterials, *International Journal of Fatigue* (2018), doi: https://doi.org/10.1016/j.ijfatigue.2018.05.006

Original article

Multiscale modeling of fatigue crack propagation in additively manufactured porous biomaterials

R. Hedayati[1,2*], H. Hosseini-Toudeshky[3], M. Sadighi[2], M. Mohammadi-Aghdam[2], A.A. Zadpoor[2]

[1]*Department of Mechanical Engineering, Amirkabir University of Technology (Tehran Polytechnic), Hafez Ave, Tehran, Iran*
[2]*Department of Biomechanical Engineering, Faculty of Mechanical, Maritime, and Materials Engineering, Delft University of Technology (TU Delft), Mekelweg 2, 2628 CD, Delft, The Netherlands*
[3]*Department of Aerospace Engineering, Amirkabir University of Technology (Tehran Polytechnic), Hafez Ave, Tehran, Iran*

[1] Corresponding author, email: r.hedayati@tudelft.nl, rezahedayati@gmail.com, Tel: +31-15-2781021.

Abstract

Advances in additive manufacturing (AM) techniques have enabled fabrication of highly porous titanium implants that combine the excellent biocompatibility of bulk titanium with all the benefits that a regular volume-porous structure has to offer (e.g. lower stiffness values comparable to those of bone). Clinical application of such biomaterials requires thorough understanding of their mechanical behavior under loading. Computational models have been therefore developed by various groups for prediction of their quasi-static mechanical properties. The fatigue behavior of AM porous biomaterials is, however, not well understood. In particular, computational models predicting the fatigue response of these structures are rare. That is primarily due to the fact that geometrical features present in computational model of fully porous structures span over multiple length scales. This makes the problem formidably expensive to solve computationally. Here, we propose a multi-scale modeling approach to alleviate this problem and solve the problem of crack propagation in AM porous biomaterials. In this approach, the area around the crack tip is modelled at the micro-scale (using beam elements) while the area far from the crack tip is modeled at the macro-scale (using volumetric elements). Compact-tension notched specimens were fabricated using a selective laser melting machine for validating the results of the presented modeling approach. The multi-scale computational model was found to be capable of predicting the fatigue response observed in experiments.

Keywords: Multi-scale model; porous biomaterial; fatigue properties; numerical modeling; additive manufacturing

1. INTRODUCTION

Advanced additive manufacturing (AM) techniques have enabled the ultimate form-freedom in designing porous biomaterials that are aimed for application as orthopedic implants. It has therefore become possible to fabricate fully porous biomaterials with regular interconnected porosities. AM porous biomaterials with such topological properties offer unique features including bone-mimicking mechanical properties [1, 2] and enlarged internal surface area that could be used for application of antibacterial coatings to prevent implant-associated infections [3]. The micro-architecture of additively manufactured porous biomaterials (unit cell type, density, pore size, etc.) regulate the mechanical [4] and biological [5, 6] response of such structures.

In the recent years, many research have studied the quasi-static mechanical properties of AM porous biomaterials based on various types of repeating unit cell types, different porosities, and varying pore sizes using analytical [7-10], numerical [11-13], and experimental [14-16] approaches. Since bone substituting implants are loaded repetitively (i.e. > 2 million times per year [17]), their fatigue response is of great clinical relevance. Most of the studies carried out on the fatigue properties of AM porous structures have been experimental [18, 19]. Recently, we developed a methodology for numerical predictions of the S-N curves of porous biomaterials subjected to compression-compression cyclic loading [20]. Porous biomaterials are primarily loaded under compression and bending. In the tensile regions of AM porous biomaterials subjected to bending, cracks may initiate and propagate. Even when the overall porous structure is purely experiencing compression, local tensile stresses might develop at the micro-scale due to the different orientation of the struts constituting the porous structure. It is therefore important to study fatigue crack propagation in AM porous biomaterials [21]. Computational prediction of the

fatigue behavior in general and crack propagation in particular is especially valuable, as it could remove the need for lengthy and expensive tests that are usually required to study the fatigue behavior of AM porous biomaterials. Moreover, computational models are required for interpreting the results of the crack propagation experiments performed on AM porous biomaterials. In the case of bulk materials, several analytical (e.g. linear elastic fracture mechanics and elastic-plastic fracture mechanics) and computational methods (e.g. singular elements and cohesive zone elements) are available for interpreting the experimental results. However, such methods are not applicable to AM porous biomaterials due to the complexity of the micro-structure of these structures. In that case, using computational micromechanics [22-28] would be very useful due to its ability to consider the complexities observed in the micro-architecture of these materials. Micro-modeling of the microstructure of porous biomaterials is efficient for relatively small structures. As the number of struts in open-cell porous structures increases, the computational effort necessary to solve the mechanical response of the porous structure increases exponentially. For objects whose sizes are large enough to enable actual application as orthopedic implants, solving the numerical micromechanical model is formidably expensive. That has been a major challenge in computational study of crack propagation in this kind of porous structures.

Here, we propose a multi-scale numerical approach for modeling crack propagation in AM porous biomaterials that could tackle the challenges associated with the computational cost of the simulations. In this approach, the area around the crack tip is modeled at the micro-scale (using beam elements) while the area far enough from the crack tip is modeled only at the macro-scale (using volumetric elements). We designed and fabricated notched compact-tension (CT) specimens using a selective laser melting (SLM) machine to perform crack propagation

experiments that were then used to validate the results obtained with the proposed numerical approach.

2. MATERIALS AND METHODS

2.1. Experimental technique

Three CT specimens with similar macro- and micro-structural topologies were manufactured from Ti-6Al-4V powder using a selective laser machine (SLM 125, Realizer, Germany) (Figure 1-2). Exposure time of 300 μs and laser current of 1200 mA were chosen for the laser beam. To better transfer load from the clamps to each CT specimen, two solid rings with appropriate dimensions were machined and inserted into the holes (Figure 1b). The dimensions of the specimens were 80 mm × 78 mm × 15 mm (Figure 1a). The lattice structure was based on cubic diamond unit cells (Figure 3). The struts had diameters of 150.71 ± 11.6 μm and lengths of 433.07 ± 7.12 μm. The micro-architecture of the CT specimens is presented in Figure 4 with different magnifications. To test the specimens under static loading, a displacement rate of 2 mm/min was applied. To test the specimens under fatigue loading, tension-tension cyclic loading with a loading ratio of $R = 0.1$ was used. The maximum load in fatigue tests was $300.1\ N$ and the test frequency was set to $15\ Hz$. Both types of tests were performed using an Instron ElectroPuls E10000 mechanical testing machine with a $10\ kN$ load cell.

Since the numerical model consists of both beam elements (for microscale region) and volumetric elements (for macroscale region), it is necessary to know what the macro-scale mechanical properties of the porous structure is. Therefore, three cylindrical samples ($D = 15\ mm$ and $L = 20\ mm$) with similar processing parameters used for manufacturing of the CT specimens were manufactured. The mechanical properties such as plateau stress, elastic modulus, and yield stress were obtained using the method explained elsewhere [29].

2.2. FE modelling of fatigue damage propagation

ANSYS implicit solver was implemented for creating the models and solving the governing equations. Timoshenko beam elements with three integration points (BEAM189 in ANSYS) were used for modelling the struts in the microscale region of the model and 8-noded brick elements (SOLID185 element type in ANSYS) were used for discretizing the macroscale region of the model. The mechanical properties of bulk Ti-6Al-4V (listed in Table 1) were used to model the mechanical behavior of the struts in the micro-scale model or the micro-scale region of the multi-scale model. For the macro-scale region, the mechanical properties obtained from porous cylindrical specimens (listed in Table 1) with micro-architectures similar to that of the CT specimens were used. The multiscale model consisted of 35,520 volumetric elements and 103,737 beam elements.

For describing the fatigue behavior of the parent material, the S-N curve presented in Figure 3 of [20] was used. In fatigue simulations, in order to decrease the computational time, the number of simulation cycles are usually smaller than the loading-unloading cycles, i.e. each simulation cycle represents a number of loading-unloading cycles, Δn_i. A preliminary study was carried out to find the optimum range for Δn_i in the FE CT specimens. The results of that preliminary study indicated that the optimum range of Δn_i in each simulation cycle should be determined according to the number of removed or degraded elements. The results of different simulations converged, if Δn_i was chosen in such a way that the number of removed elements in each simulation cycle was no more than 0.001% of the total number of elements.

In the multi-scale model, the micro-scale region was extended when the crack tip grew too close to the interface frame (between the micro-scale and macro-scale regions). Since in open-cell structures, the crack tip is blunt (i.e. we have a damage area in open-cell porous structures

instead of a crack tip in solid materials), the concept of crack "tip" is not directly applicable. Instead, the mean XY location of the removed elements in the cycle was calculated at the end of each simulation cycle. If the distance between the damage area and the interface frame was smaller than 4 cells, the micro-scale area was enlarged by three cells in all directions.

To better simulate the actual load transfer from clamps to the porous structure, the solid clamps were modeled with cylindrical shapes (Figure 5b) and were assigned the mechanical properties of Ti-6Al-4V. The cylinders (which were representatives of clamps) were discretized in such a way that there were always nodes in their central axes (by adding hard points to their central axis before meshing them in ANSYS). All the DOFs of the nodes located in the central axis of the lower clamps were constrained. The DOFs of the nodes located in the central axis of the upper clamp were given a displacement only in the Z direction and were not allowed to move in the X and Y directions (Figure 5).

2.2.1. Consideration of damage accumulation in elements

To calculate the damage accumulated in the struts (in the micro-scale model or in the micro-scale region of the multi-scale model), the Miner's rule $D = \sum_i \frac{\Delta n_i}{N_i}$ [30] was used. Using the S-N curve of the parent material, the life N_i of the material for the equivalent stress level of each strut was obtained. The accumulated damage in the material for the simulation cycle i was equal to $\frac{\Delta n_i}{N_i}$.

After struts fail one by one in the lattice structure, they lose their contribution to the load bearing of the porous structure. As a result, the elastic modulus of the lattice structure decreases. Moreover, the stiffness of the lattice structure decreases even before any strut has completely failed. That is because as the lattice structure goes under cyclic loading, the damage accumulated

in the struts decreases the stiffness of the struts and as a result the lattice structure. As suggested in [31, 32] and shown in [20], the elastic modulus of a deteriorated material could be obtained as:

$$\tilde{E}_{i,j} = E_s(1 - \mathrm{D}_{i,j}) \quad (1)$$

where $\tilde{E}_{i,j}$ is the elastic modulus of strut i and $D_{i,j}$ is the accumulated damage in strut i (both corresponding to the simulation cycle j). In the FE model, twenty different material models with different elastic moduli ranging from 0 to the initial elastic modulus of the bulk material were created and assigned to different elements at each cycle numbers according to their current damage value (using Eq. (1)).

2.2.2. The implementation of S-N diagram

The S-N curves are usually obtained for completely reversible loads. Since the applied stress was not completely reversible and it was tensional-tensional with a loading ratio of $R = 0.1$, the following relationship (based on the modified version of the Goodman's relationship [20, 33, 34]) was used for converting the fluctuating stress to equivalent reversible stress:

$$\sigma_{rev} = \frac{\sigma_a}{1 - \frac{\sigma_m}{S_{ut}}} \quad (2)$$

where σ_a and σ_m are respectively the amplitude and mean values of the fluctuating stress and S_{ut} is the ultimate stress of the bulk material in tension. Since in this study $R = 0.1$, we have $\sigma_a = 0.45\,\sigma_{max}$, and $\sigma_m = 0.55\,\sigma_{max}$, which gives [20]:

$$\sigma_{rev} = \frac{0.45\,\sigma_{max}}{1 - \frac{0.55\,\sigma_{max}}{S_u}} \quad (3)$$

The stress concentration factor linearly decreases the slope of the LogS-LogN diagram from the point $(0, \log S_u)$ (with a minimum drop of zero) to the point $(N_e, \log S_e)$ (with a maximum drop of $K_{f,max}$), where N_e is the cycle number at the beginning of the endurance limit region. In [20],

we showed that the equation for the S-N curve after applying stress concentration factor can be obtained by replacing N in the original S-N diagram by

$$N = 10^{f\left(\frac{-b+\sqrt{b^2+4aLog(S)}}{2a}\right)} \quad (4)$$

where $= \frac{1-K_{f,max}}{T_e-T_u}$, $b = 1 - aT_e$, $T_u = \log(S_u)$, $T_e = \mathrm{Log}(S_e)$, and function f is the equation describing the original LogN-LogS curve (which is the logarithmic N-S curve).

2.2.3. Irregularities in strut cross-sections

To consider the irregularities in the micro-scale model and the micro-scale region of the multi-scale model, different cross-sections sizes were assigned to different struts. The cross-section size of each strut was chosen from a Gaussian distribution with the mean and standard deviation values equal to the corresponding measured values obtained from the manufactured specimens. 21 cross-section sizes were chosen for the struts (1 cross-section size equal to the mean cross-section of manufactured specimens, 10 cross-sections larger than mean value, and 10 ones smaller).

The irregularities created during the AM of the porous structure increases the local stress values in the struts not only because the cross-section area of some parts of the struts are very small but also because very small curvatures in the surface of the struts create stress concentration. Due to unavailability of data regarding the statistical distribution of the stress concentration factors, one stress concentration factor was used for all the struts of a structure. To implement the stress concentration concept in the fatigue problem, after each solution, the stress obtained in each strut was multiplied by K_f before being used in the damage accumulation relationship (i.e. Miner's rule). An iterative procedure was used to determine the effective K_f. In this approach, first an arbitrary value of K_f was chosen for each structure and the fatigue life was obtained for

$F = 0.5\ F_y$, where F_y is the load at which the quasi-static load-displacement curve becomes non-linear for the first time (equivalent to yield load in the load-displacement curve of cylindrical specimens under axial loading). The K_f value was then modified according to the fatigue life obtained for this initial value. This procedure was repeated until the numerical fatigue life was close to the fatigue life obtained from experiments. The K_f value obtained for $F = 0.5\ F_y$ was used for other applied loads too.

2.2.4. The damage propagation algorithm

The algorithms used to model the progressive damage in the micro-scale or multi-scale models were similar (Figure 7a shows the flowchart used for modeling progressive damage in both models). Depending on the type of analysis (i.e. micro-scale or multi-scale), some blocks of the flowchart shown in Figure 7a were replaced by the flowchart blocks shown in Figure 7b-d. Flowchart in Figure 7a specifies where and how the noted blocks should be replaced. One of the main difficulties encountered during the multi-scale modeling was coupling the neighboring nodes of the beam elements (in micro-scale model) and volumetric elements (in macro-scale model) at the interface between the micro-scale and macro-scale parts of the multi-scale model. The micro- and macro-scale regions were discretized in such a way that for each node of the micro-scale model located in the micro-macro interface frame, there was a corresponding node from the volumetric elements in the macro-scale region. Using the coupling command to constraint the degrees of freedom (DOFs) of the adjacent nodes of the micro-scale and macro-scale models in the interface between the two noted regions led to solution errors due to development of negative pivots in the stiffness matrix created in ANSYS FE code. To resolve this, for each beam element with one of its nodes located in the micro-macro interface area, the XYZ locations of its end nodes were stored, the node number of the adjacent volumetric element

was specified, the noted beam element was removed, and a new beam element was created. In each newly created beam element, the node located in the interface area belonged to the volumetric element and the node in its other end belonged to the previous (deleted) beam element. This process is called merging in the flowchart presented in Figure 7b.

3. RESULTS

The static force-displacement curve was initially linear until it reached a maximum point after which it showed a severe decrease (Figure 9a). While the rising part of the curve was smooth, the falling part of the curve was non-smooth and had several fluctuations. The sharp peaks in the falling region of the force-displacement curve (Figure 9a) represent the crack propagation from one unit cell to the next. The crack propagation under different applied displacements is shown in Figure 10. In most specimens, the crack propagation pathway was almost straight and made a 20° angle with the notch direction (Figure 10).

In the fatigue experiments, the displacement-cycle diagrams were bilinear similar to what was observed in the corresponding curves in [20] for porous cylindrical samples under compression-compression load. In the first stage, the displacement increased slowly up to a critical point after which the displacement increased rapidly (Figure 9b). The fatigue lives in all the specimens were close and in the logarithmic range of 6000-12000 cycles. The final fracture in all specimens occurred in displacements around or less than 0.8 mm. In other words, the displacement-cycle diagrams became vertically asymptotic once the displacement reached 0.8 mm.

The solution time for the multi-scale model demonstrated in Figure 5 was very high and each simulation cycle took about 0.5-1 h using a computer with 16 GB RAM and Core i7 CPU. The simulation results showed that the results do not converge, if the number of removed elements in each simulation cycle exceeds 12. The fatigue life obtained for each specimen was strongly

dependent on the value of the surface factor (stress concentration factor). A small change in the surface factor altered the fatigue life significantly. The curve plotted in Figure 9b corresponds to a surface factor of 0.85. It took about 4 months to reach the numerical curve plotted in Figure 9b. For fitting purposes, the horizontal axis of the multi-scale FE model (in Figure 9b) has been divided by 1.74.

4. DISCUSSIONS

We proposed a multi-scale modeling approach that enabled prediction of the fatigue response of CT specimens. Corresponding experiments were also performed to validate the simulation results. There was generally a good agreement between the simulation and experimental results.

4.1. Differences with compression-compression fatigue from FE modelling point of view

In our previous study [20], we investigated damage development in porous structures subjected compressive cyclic loading. The algorithm used in this study for modelling damage propagation in CT specimens under tension-tension loading had some similarities with the one used in [20]. For example, the FE model took into account the irregularity in the cross-section area and stress concentration factors. However, during the multi-scale FE model development process of CT specimen, several challenges were faced, which showed that other factors have to be also taken into account when modeling damage propagation in CT specimens using multiscale FE models. For example, in the cylindrical specimens under compression-compression loading, when the elements were considered to be damaged ($d = 1$), their material properties were changed to a very small value (e.g. $E_s = 1\ Pa$). This method helped to better visualize the damage extent inside the lattice structure. This methodology of "removing" elements was however unsuccessful in the CT multi-scale model used in this study and led to numerical errors and solution divergence after the first simulation step. This was due to the fact that in the CT models studied

here, the damage area is concentrated around the crack tip, and the development of an area of beam elements with negligible stiffness in the neighborhood of an area of beam elements with very high stiffness leads to the presence of small pivot terms in the stiffness matrix of the model. In the cylindrical models under compression-compression loading, the elements with negligible stiffness values are distributed throughout the whole structure, such problems were not encountered until the very final moments of the fatigue problem solution when the majority of the elements were removed. In the CT model, to remove each element, the element had to be actually removed from the model.

In compressive loading, the compression plate loads could be applied by two approaches. In the first approach, the cylindrical geometry of the compression plates were constructed in the FE model and contact algorithm was defined between the compression plates and the cylindrical porous structure. Adding contact algorithm to the FE model made numerical solution much more complex and, in many cases, led to unexpected solution errors. An alternative approach was therefore used to apply boundary and loading conditions in the compression-compression problem. In this approach, the nodes located at the lowermost part of the porous structure were constrained in the vertical direction and the nodes located at the top surface of the porous structure were given a specified downward displacement. As for the multiscale modeling of CT specimens, using the first approach (i.e. defining contact algorithm between the holes of the CT specimen and the pins of the clamps) led to similar solution problems. Using the second method (i.e. constraining all the nodes of the porous structure located in the periphery of the lower hole position and displacing the nodes of the porous structure located in the periphery of the top hole in the Y direction) created unrealistic loading and boundary conditions which were not experienced in actual tests. In the experimental tests, different points in the periphery of the CT

specimen holes could have different vertical displacements (due to relative rotational movement of the holes in contact with clamp pins). In fact, the center of the holes had a predefined pure upward movement with a displacement rate predefined by the user, while the contour around the holes experienced different vertical displacements. To create a more realistic loading and boundary condition in the hole contours, the holes were filled by much stiffer cylinders (the outer boundaries of which were merged with the boundaries of the holes), and the boundary and external loading conditions were applied to the central axes of the noted stiff cylinders only.

In our previous study [20], it was seen that under compressive loading, using multi-linear material model instead of linear elastic material model does not significantly change the observed behavior of the porous structure (such as the resulted S-N curve, displacement-cycle curve, etc.). This was due to the fact that in cylindrical specimens in high cycle fatigue condition ($\sigma_{max} \leq 0.6\ \sigma_y$), inelastic behavior in the material occurs only in the uneven outer surfaces of the struts and the internal parts of the struts remain always elastic. In fact, in compression-compression loading, the propagation of micro-cracks in the struts under "elastic" stress conditions is the main cause of damage accumulation in the porous structures. In the CT specimens, however, the struts located close to the crack tip are usually in the plastic regime. If the plasticity is ignored in the CT numerical model, the stress in area around the crack tip becomes very high and the damage area spreads unrealistically fast leading to unacceptable results.

4.2. Other FE modelling considerations

In our numerical model, the micro- and macro-scale regions were connected to each other through the common nodes between them. This increased the stress concentration in the regions very close to the interface frame. More accurate approaches may be needed in some cases when

trying to connect beam elements to volumetric elements, as the nodes of beam elements have 6 DOFs (three translations and three rotations) while the nodes of the volumetric elements have 3 DOFs (three translations). In our multi-scale model, the end nodes of the beam elements were simply connected to the corresponding volumetric elements. Since the distance between the interface region and the crack tip was always at least four unit cells and as the damaged area did not approach the interface area, simply connecting the beam and volumetric elements was effective in the case of our simulations. However, using a multiple constraint approach may further improve the accuracy of the model in the interface area and decrease the stress concentration observed in that region.

An alternative method would be to create two separate micro-scale and macro-scale models: a complete CT model wholly made of volumetric elements (with the mechanical properties of the porous structure) and a micro-scale model representative of the area around the crack tip. After solving the complete macro-scale CT model, the nodal forces in the hypothetical interface frame could be calculated and transferred to the micro-scale model. The micro-scale model could then be solved using the forces obtained from the macroscale model to allow the crack to propagate. While this method of transferring the loads from the macro-scale model to the micro-scale model decreases the artificial stress concentration at the interface frame area, it only gives acceptable results in the initial steps of the damage propagation. Once the crack has substantially propagated, the loads obtained from the macro-scale model are not accurate anymore, because the effects of the new state of the crack are not reflected in the macro-scale CT model.

4.3. Micro- vs. multi-scale models

The multi-scale model showed several advantages over the micro-scale model. First, the computational time in the multi-scale model was much smaller than in the micro-scale model (30

min vs. 90 min using a PC computer with 16 GB RAM and Core i7 CPU). Computers with less performance capacities (e.g. a laptop computer with 8 GB RAM and Core i7 1.8 GHz CPU) were able to solve the multi-scale model but unable to solve the micro-scale model. In the micro-scale model, in order to have a clamping condition similar to that experienced in the experimental tests, using contact algorithms between the porous structure and the clamps would be inevitable. In the multi-scale model, the area far from the crack tip was discretized using volumetric elements. Merging the hypothetical clamping and the (volumetric meshed region of the) porous structure was therefore possible, resulting in more accurate results. The stress distribution observed in the area around the crack tip was similar for both models when the loading and boundary conditions of the multi- and micro-scale CT models were similar.

4.4. Application in biomedical implants

The load-bearing implants inside the body are usually loaded in compression and bending, because they usually have to sustain the body weight. There are several works [35-37] that have reported the failure of the implants in Mode-I crack propagation. The neck [37], the stem-sleeve interface [38], and the body [35] of the femoral component stems have all been reported as the fracture sites after implantation. Microscopic examination of the fracture surface has in most cases revealed that the fracture has been caused by fatigue loading (for example the presence of dark corroded area representing the fracture initiation sites and concentric clamshell marks representative of fatigue failure) [35-38]. In tension or bending, the mode-I fatigue fracture propagation is very dependent on the micro-features of the structure. Due to the nature of the micro-structure of AM porous biomaterials, the locations with very high stress concentration factors are much more abundant in those structures as compared to solid implants. AM porous biomaterials are therefore more vulnerable to fatigue fracture. Taking into account the

complexities in stress distribution in the micro-structure of porous structures (which depends on several factors such as unit cell size, unit cell shape, roughness of the struts, etc.), a micro-mechanical approach is expected to yield much more accurate results as compared to a macro-mechanical model. By modeling the micro-structure of the entire porous structure, the computational analysis time will increase substantially. The multi-scale methodology proposed in this study combines the best of both approaches and results in an accurate prediction of the fatigue behavior within a more reasonable time frame.

5. CONCLUSIONS

In this study, a multi-scale computational approach was proposed to predict crack propagation in AM porous biomaterials. CT specimens were also manufactured from AM porous biomaterials and tested under fatigue. The results of the multi-scale computational model matched those found in the experiments. The multi-scale models had several advantages over the micro-scale model including much smaller computational time, much better prediction of stress distribution in crack tip region, and less solution instabilities. The preprocessing procedure for the multi-scale model was, however, more complex. The results of this study also showed that considering plasticity in the material behavior of the parent material is of great importance, since the struts located around the crack tip are usually in the plastic regime. This is in contrary to cylindrical porous structures under compression-compression loading studied in our previous study which showed that considering either linear elastic or elastic-plastic material models yields similar results especially for lower stress levels .

REFERENCES

1. Bobbert, F., K. Lietaert, A. Eftekhari, B. Pouran, S. Ahmadi, H. Weinans, and A. Zadpoor, *Additively manufactured metallic porous biomaterials based on minimal surfaces: A unique combination of topological, mechanical, and mass transport properties.* Acta Biomaterialia, 2017.

2. Zadpoor, A.A. and R. Hedayati, *Analytical relationships for prediction of the mechanical properties of additively manufactured porous biomaterials.* Journal of Biomedical Materials Research Part A, 2016. **104**(12): p. 3164–3174.
3. Amin Yavari, S., L. Loozen, F.L. Paganelli, S. Bakhshandeh, K. Lietaert, J.A. Groot, A.C. Fluit, C. Boel, J. Alblas, and H.C. Vogely, *Antibacterial behavior of additively manufactured porous titanium with nanotubular surfaces releasing silver ions.* ACS applied materials & interfaces, 2016. **8**(27): p. 17080-17089.
4. Ahmadi, S., R. Hedayati, Y. Li, K. Lietaert, N. Tümer, A. Fatemi, C. Rans, B. Pouran, H. Weinans, and A. Zadpoor, *Fatigue performance of additively manufactured meta-biomaterials: The effects of topology and material type.* Acta biomaterialia, 2018. **65**: p. 292-304.
5. Van Bael, S., Y.C. Chai, S. Truscello, M. Moesen, G. Kerckhofs, H. Van Oosterwyck, J.-P. Kruth, and J. Schrooten, *The effect of pore geometry on the in vitro biological behavior of human periosteum-derived cells seeded on selective laser-melted Ti6Al4V bone scaffolds.* Acta biomaterialia, 2012. **8**(7): p. 2824-2834.
6. Taniguchi, N., S. Fujibayashi, M. Takemoto, K. Sasaki, B. Otsuki, T. Nakamura, T. Matsushita, T. Kokubo, and S. Matsuda, *Effect of pore size on bone ingrowth into porous titanium implants fabricated by additive manufacturing: an in vivo experiment.* Materials Science and Engineering: C, 2016. **59**: p. 690-701.
7. Hedayati, R., M. Sadighi, M. Mohammadi-Aghdam, and A. Zadpoor, *Analytical relationships for the mechanical properties of additively manufactured porous biomaterials based on octahedral unit cells.* Applied Mathematical Modelling, 2017. **46**: p. 408-422.
8. Hedayati, R., A. Leeflang, and A. Zadpoor, *Additively manufactured metallic pentamode meta-materials.* Applied Physics Letters, 2017. **110**(9): p. 091905.
9. Hedayati, R., M. Sadighi, M. Mohammadi-Aghdam, and A. Zadpoor, *Mechanical properties of additively manufactured octagonal honeycombs.* Materials Science and Engineering: C, 2016. **69**: p. 1307-1317.
10. Babaee, S., B.H. Jahromi, A. Ajdari, H. Nayeb-Hashemi, and A. Vaziri, *Mechanical properties of open-cell rhombic dodecahedron cellular structures.* Acta Materialia, 2012. **60**(6): p. 2873-2885.
11. Kadkhodapour, J., H. Montazerian, A.C. Darabi, A. Zargarian, and S. Schmauder, *The relationships between deformation mechanisms and mechanical properties of additively manufactured porous biomaterials.* Journal of the mechanical behavior of biomedical materials, 2017. **70**: p. 28-42.
12. Kadkhodapour, J., H. Montazerian, A.C. Darabi, A. Anaraki, S. Ahmadi, A. Zadpoor, and S. Schmauder, *Failure mechanisms of additively manufactured porous biomaterials: Effects of porosity and type of unit cell.* Journal of the mechanical behavior of biomedical materials, 2015. **50**: p. 180-191.
13. Lohfeld, S., S. Cahill, H. Doyle, and P. McHugh, *Improving the finite element model accuracy of tissue engineering scaffolds produced by selective laser sintering.* Journal of Materials Science: Materials in Medicine, 2015. **26**(1): p. 38.
14. Bandyopadhyay, A., F. Espana, V.K. Balla, S. Bose, Y. Ohgami, and N.M. Davies, *Influence of porosity on mechanical properties and in vivo response of Ti6Al4V implants.* Acta biomaterialia, 2010. **6**(4): p. 1640-1648.
15. Hedayati, R., S. Ahmadi, K. Lietaert, B. Pouran, Y. Li, H. Weinans, C. Rans, and A. Zadpoor, *Isolated and modulated effects of topology and material type on the mechanical properties of additively manufactured porous biomaterials.* Journal of the mechanical behavior of biomedical materials, 2018.
16. Wang, X., S. Xu, S. Zhou, W. Xu, M. Leary, P. Choong, M. Qian, M. Brandt, and Y.M. Xie, *Topological design and additive manufacturing of porous metals for bone scaffolds and orthopaedic implants: A review.* Biomaterials, 2016. **83**: p. 127-141.
17. Silva, M., E.F. Shepherd, W.O. Jackson, F.J. Dorey, and T.P. Schmalzried, *Average patient walking activity approaches 2 million cycles per year: pedometers under-record walking activity.* The Journal of arthroplasty, 2002. **17**(6): p. 693-697.

18. Leuders, S., M. Thöne, A. Riemer, T. Niendorf, T. Tröster, H. Richard, and H. Maier, *On the mechanical behaviour of titanium alloy TiAl6V4 manufactured by selective laser melting: Fatigue resistance and crack growth performance.* International Journal of Fatigue, 2013. **48**: p. 300-307.
19. Barriuso, S., J. Chao, J. Jiménez, S. García, and J. González-Carrasco, *Fatigue behavior of Ti6Al4V and 316 LVM blasted with ceramic particles of interest for medical devices.* Journal of the mechanical behavior of biomedical materials, 2014. **30**: p. 30-40.
20. Hedayati, R., M. Sadighi, M. Mohammadi-Aghdam, and A.A. Zadpoor, *Computational prediction of the fatigue behavior of additively manufactured porous metallic biomaterials* International journal of fatigue, 2016. **84**: p. 67–79.
21. Hedayati, R., S.A. Yavari, and A. Zadpoor, *Fatigue crack propagation in additively manufactured porous biomaterials.* Materials Science and Engineering: C, 2017. **76**: p. 457-463.
22. Rammerstorfer, F.G., Bohm. H.J., *Composite engineering*. 2002, Vienna University of Technology: Institute of Lightweight Structures and Aerospace Engineering.
23. Ableidinger, A., *Some aspects of the fracture behavior of metal foams*. 2000: na.
24. Schaffner, G., X.-D.E. Guo, M.J. Silva, and L.J. Gibson, *Modelling fatigue damage accumulation in two-dimensional Voronoi honeycombs.* International Journal of Mechanical Sciences, 2000. **42**(4): p. 645-656.
25. Choi, S. and B.V. Sankar, *A micromechanical method to predict the fracture toughness of cellular materials.* International journal of solids and structures, 2005. **42**(5): p. 1797-1817.
26. Lee, S.-J., J. Wang, and B.V. Sankar, *A micromechanical model for predicting the fracture toughness of functionally graded foams.* International journal of solids and structures, 2007. **44**(11): p. 4053-4067.
27. Demiray, S., W. Becker, and J. Hohe, *Investigation of the fatigue behavior of open cell foams by a micromechanical 3-D model.* Materials Science and Engineering: A, 2009. **504**(1): p. 141-149.
28. Mangipudi, K. and P. Onck, *Multiscale modelling of damage and failure in two-dimensional metallic foams.* Journal of the Mechanics and Physics of Solids, 2011. **59**(7): p. 1437-1461.
29. Hedayati, R., M. Sadighi, M. Mohammadi-Aghdam, and A. Zadpoor, *Mechanical behavior of additively manufactured porous biomaterials made from truncated cuboctahedron unit cells.* International Journal of Mechanical Sciences, 2016. **106**: p. 19-38.
30. Miner, M.A., *Cumulative damage in fatigue.* Journal of applied mechanics, 1945. **12**(3): p. 159-164.
31. Lemaitre, J., *A continuous damage mechanics model for ductile fracture.* Journal of Engineering Materials and Technology, 1985. **107**(1): p. 83-89.
32. Lemaitre, J. and H. Lippmann, *A course on damage mechanics*. Vol. 2. 1996: Springer Berlin.
33. Goodman, J., *Mechanics applied to engineering*. 1919: Longmans, Green.
34. *Goodman relation*. 2015; Available from: http://en.wikipedia.org/wiki/Goodman_relation.
35. Ishaque, B.A., H. Stürz, and E. Basad, *Fatigue fracture of a short stem hip replacement: a failure analysis with electron microscopy and review of the literature.* The Journal of arthroplasty, 2011. **26**(4): p. 665. e17-665. e20.
36. Norman, P., S. Iyengar, I. Svensson, and G. Flivik, *Fatigue fracture in dual modular revision total hip arthroplasty stems: failure analysis and computed tomography diagnostics in two cases.* The Journal of arthroplasty, 2014. **29**(4): p. 850-855.
37. Grivas, T.B., O.D. Savvidou, S.A. Psarakis, P.-F. Bernard, G. Triantafyllopoulos, I. Kovanis, and P. Alexandropoulos, *Neck fracture of a cementless forged titanium alloy femoral stem following total hip arthroplasty: a case report and review of the literature.* Journal of medical case reports, 2007. **1**(1): p. 1-7.
38. Parisi, T., B. Burroughs, and Y.M. Kwon, *Modular Hip Implant Fracture at the Stem-Sleeve Interface.* Orthopedics, 2015. **38**(3): p. e234-e239.

Tables

Table 1- Mechanical properties of bulk Ti-6Al-4V and porous structure used for modeling the mechanical behavior of the multi-scale model

Property	**Solid Ti-6Al-4V**	**Porous structure**
Elastic modulus	122.3 GPa	0.22
Poisson's ratio	0.342	0.1
Tangent modulus	1.25 GPa	-
Yield stress	1000 MPa	-
Ultimate tensile strength	1200 MPa	-

Figures

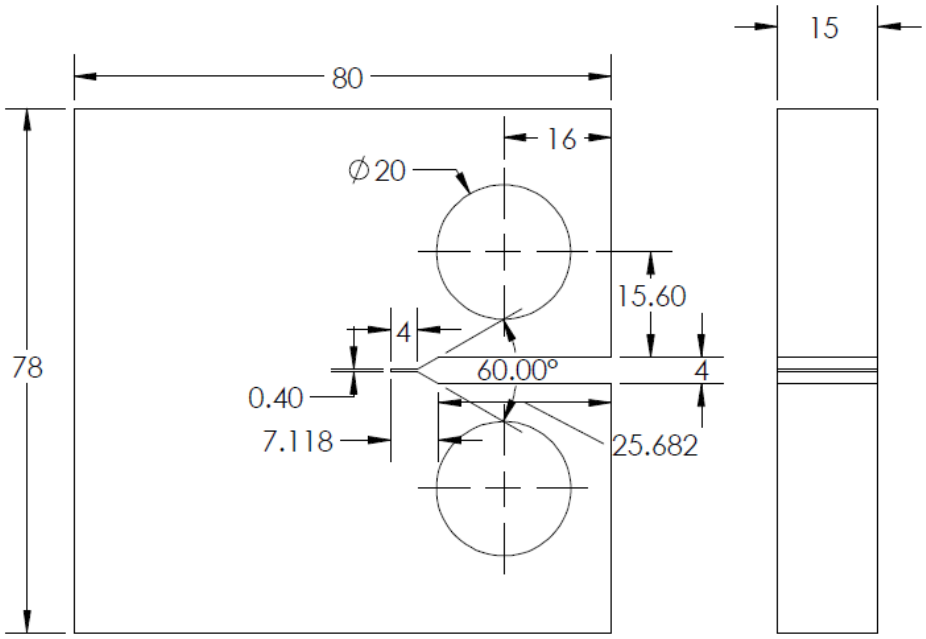

(a)

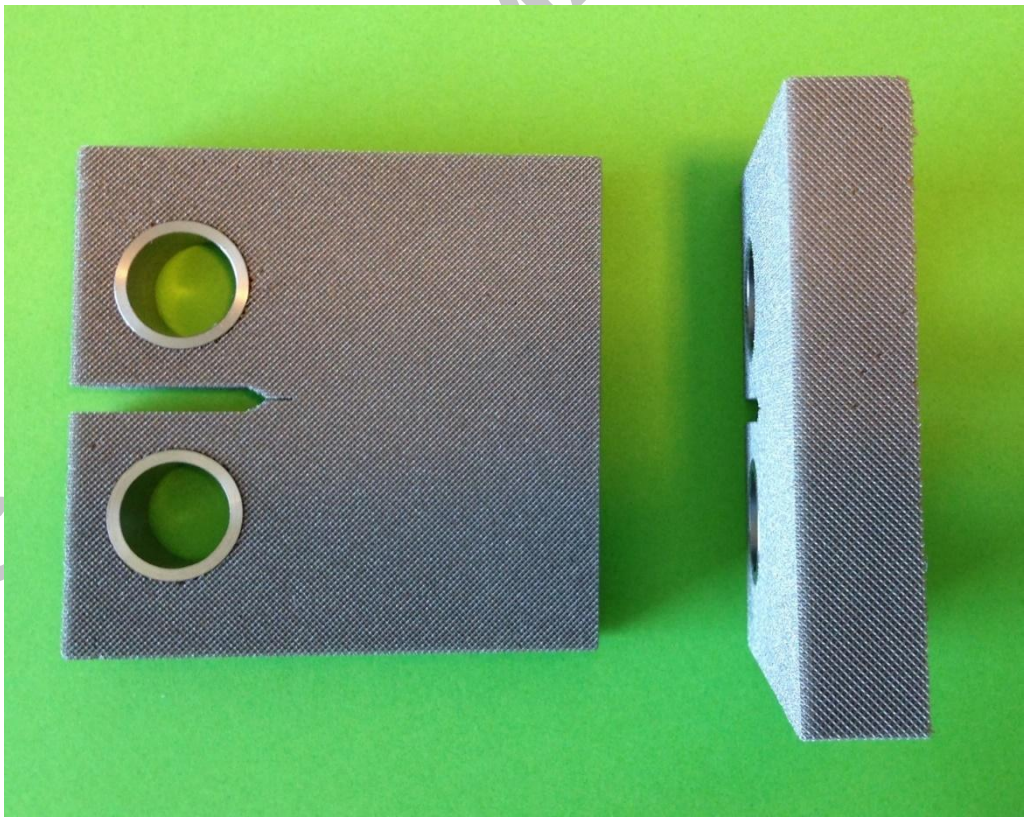

(b)

Figure 1- (a) The dimensions of the CT specimens (b) The manufactured CT specimens from two views

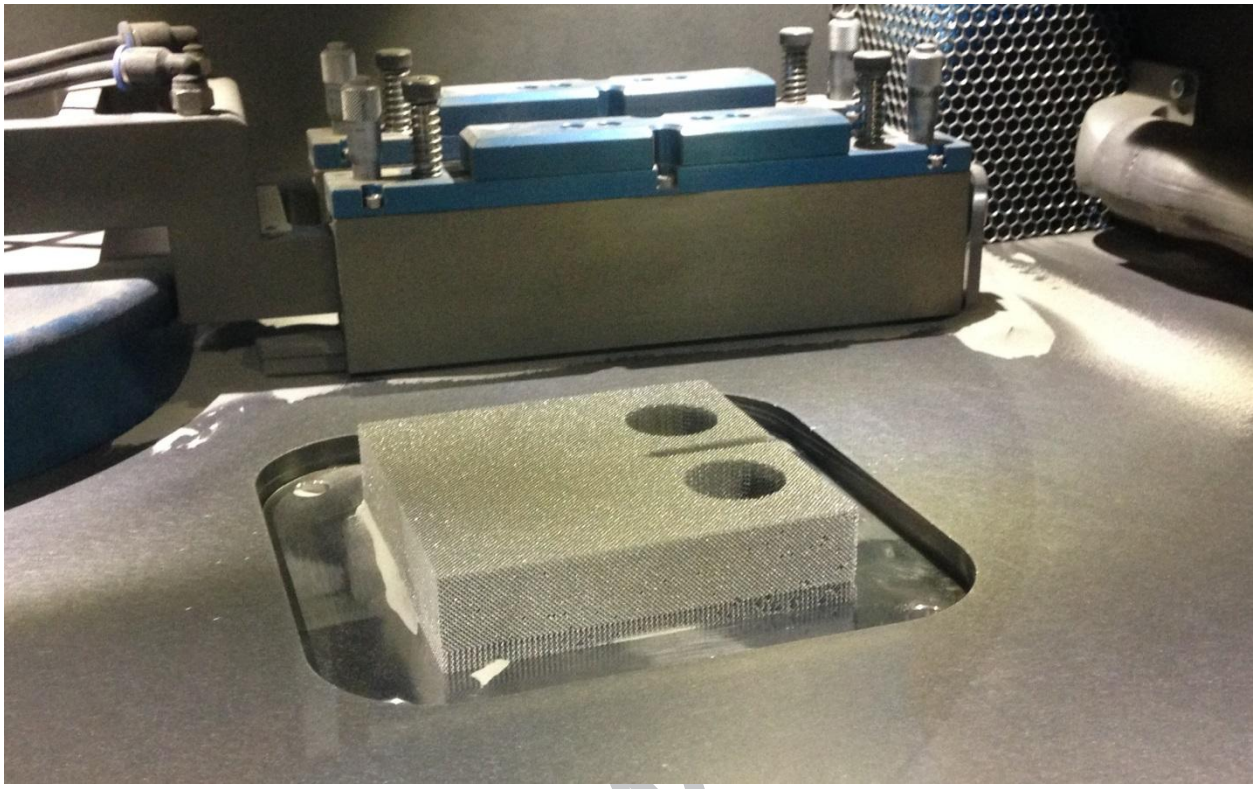

Figure 2- A view of the additively manufactured CT specimen in the SLM machine

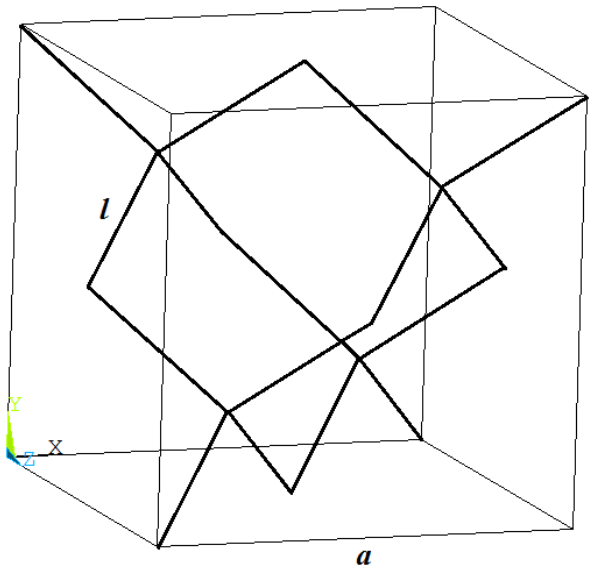

a = 1 mm
l=0.433 mm

Figure 3- The diamond unit cell (the bold lines) used for creating the micro-scale geometry of the lattice structure

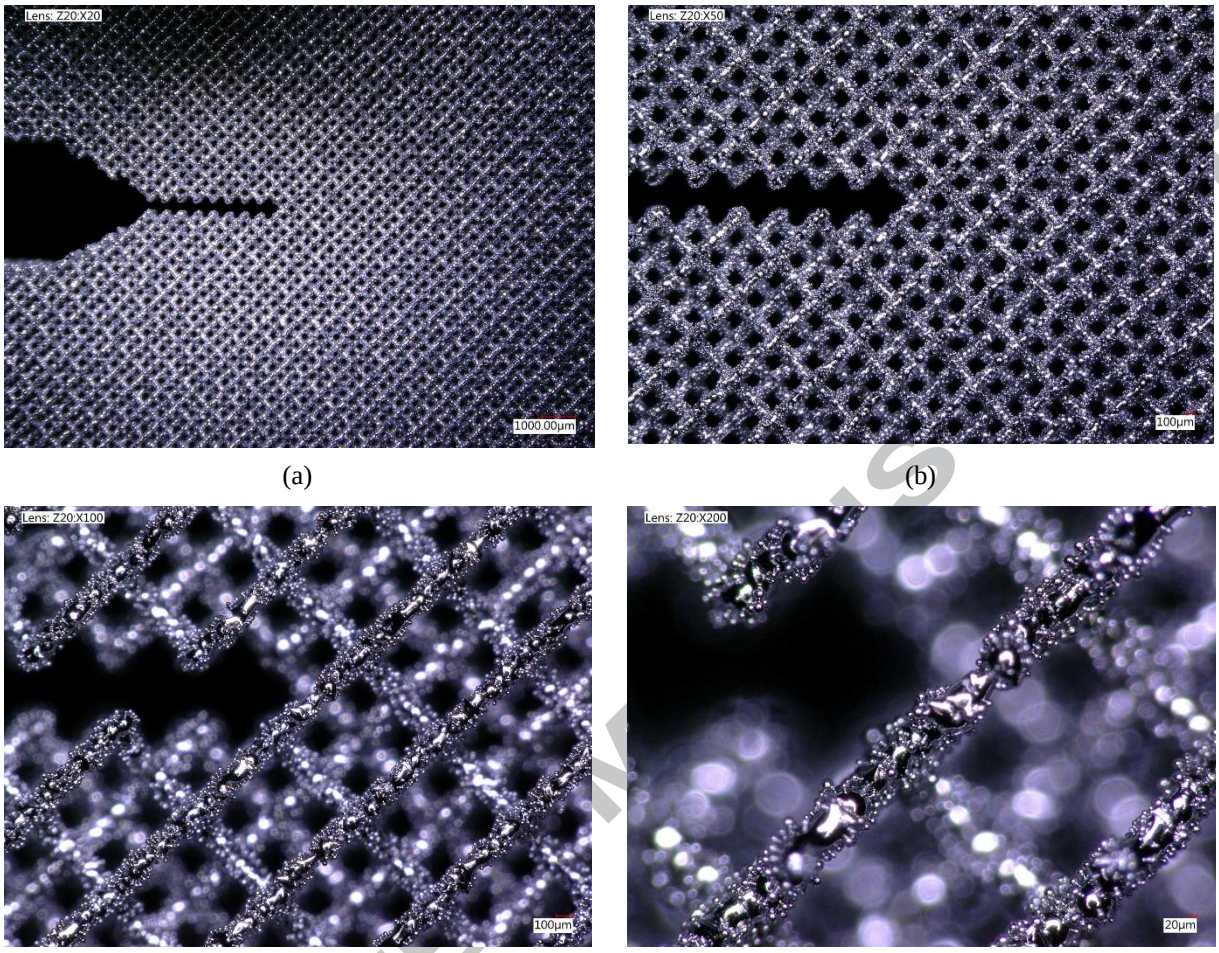

Figure 4- Microscopic views of notch tip for (a) 20X, (b) 50X, (c) 100X, and (d) 200X magnifications

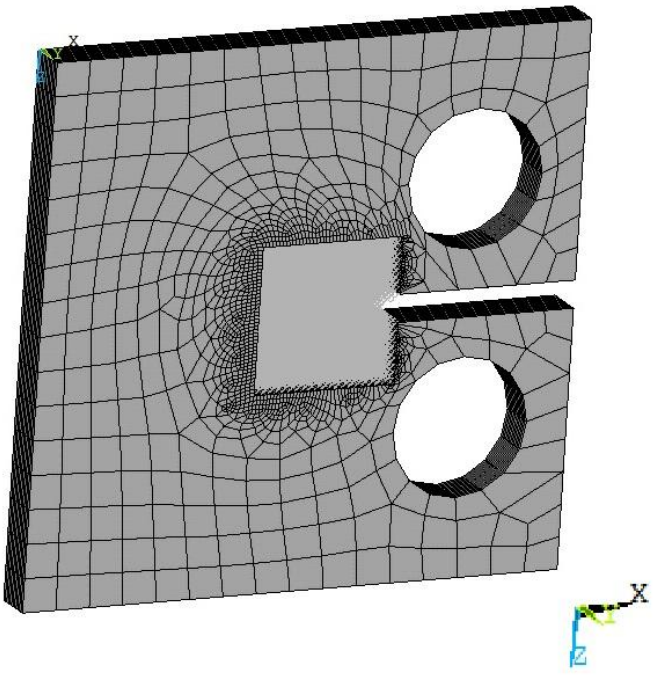

(a)

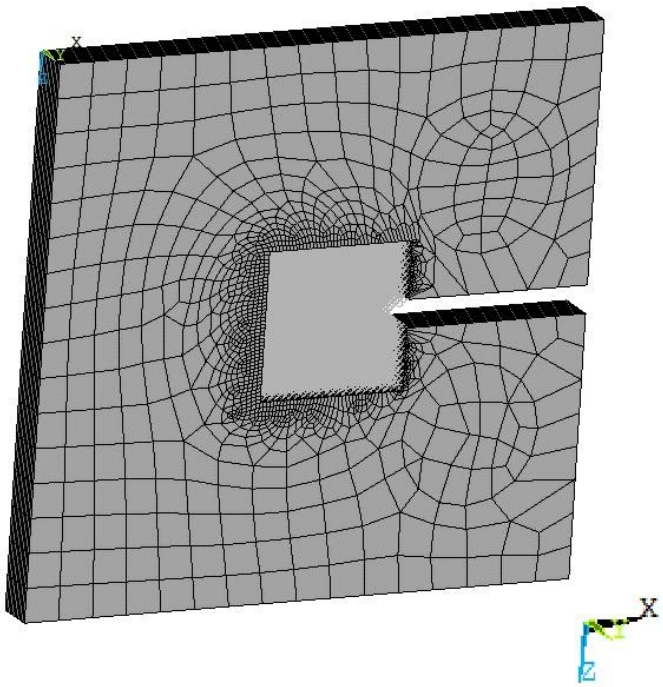

(b)

Figure 5- (a) A 3D view of the multi-scale FE model; (b) Implementation of extra cylinders to model the loading condition in the clamping area

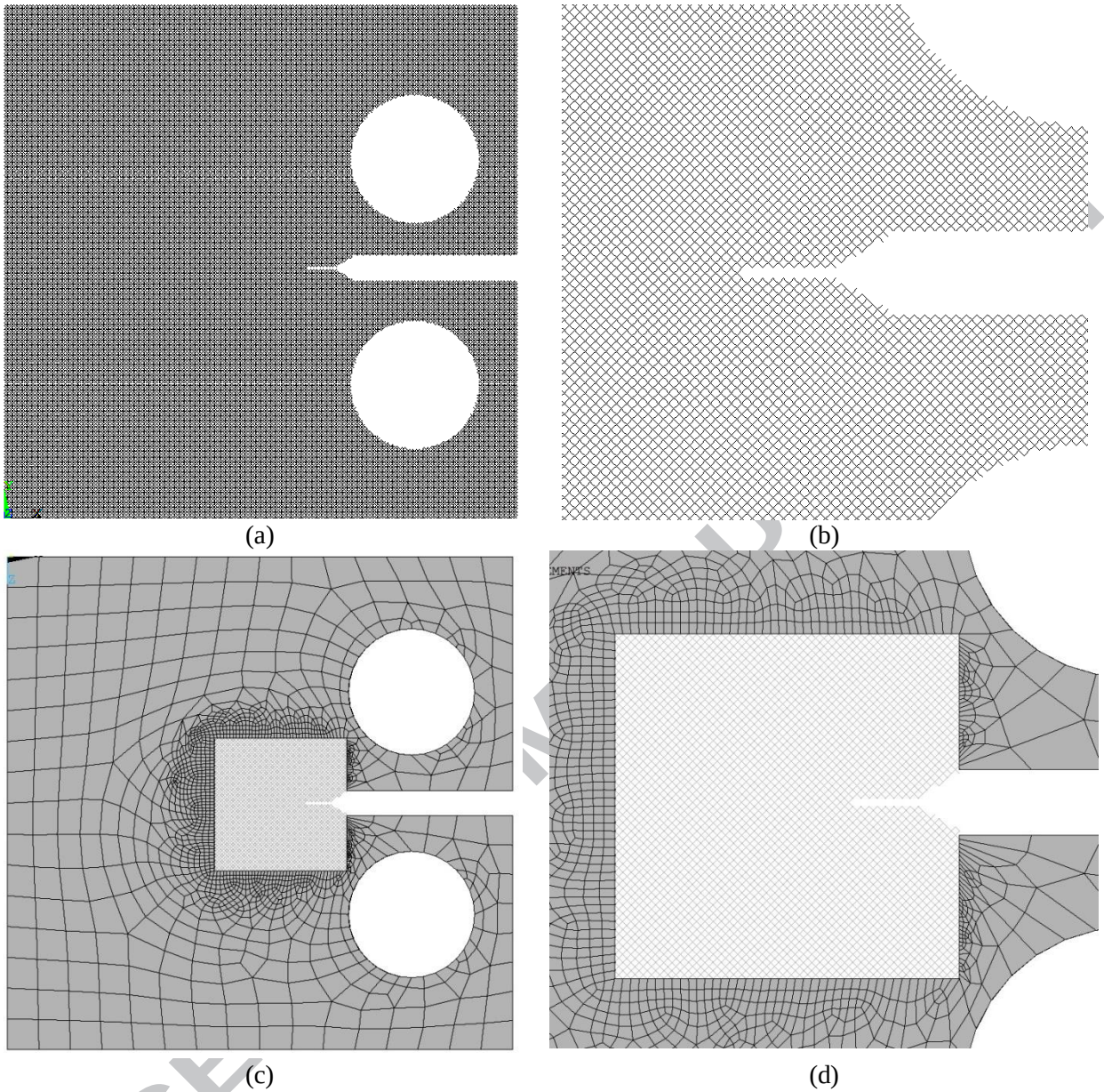

Figure 6- (a) The whole micro-scale model, (b) the crack tip area in micro-scale model, (c) The whole multi-scale model, and (d) the crack tip area in multi-scale model

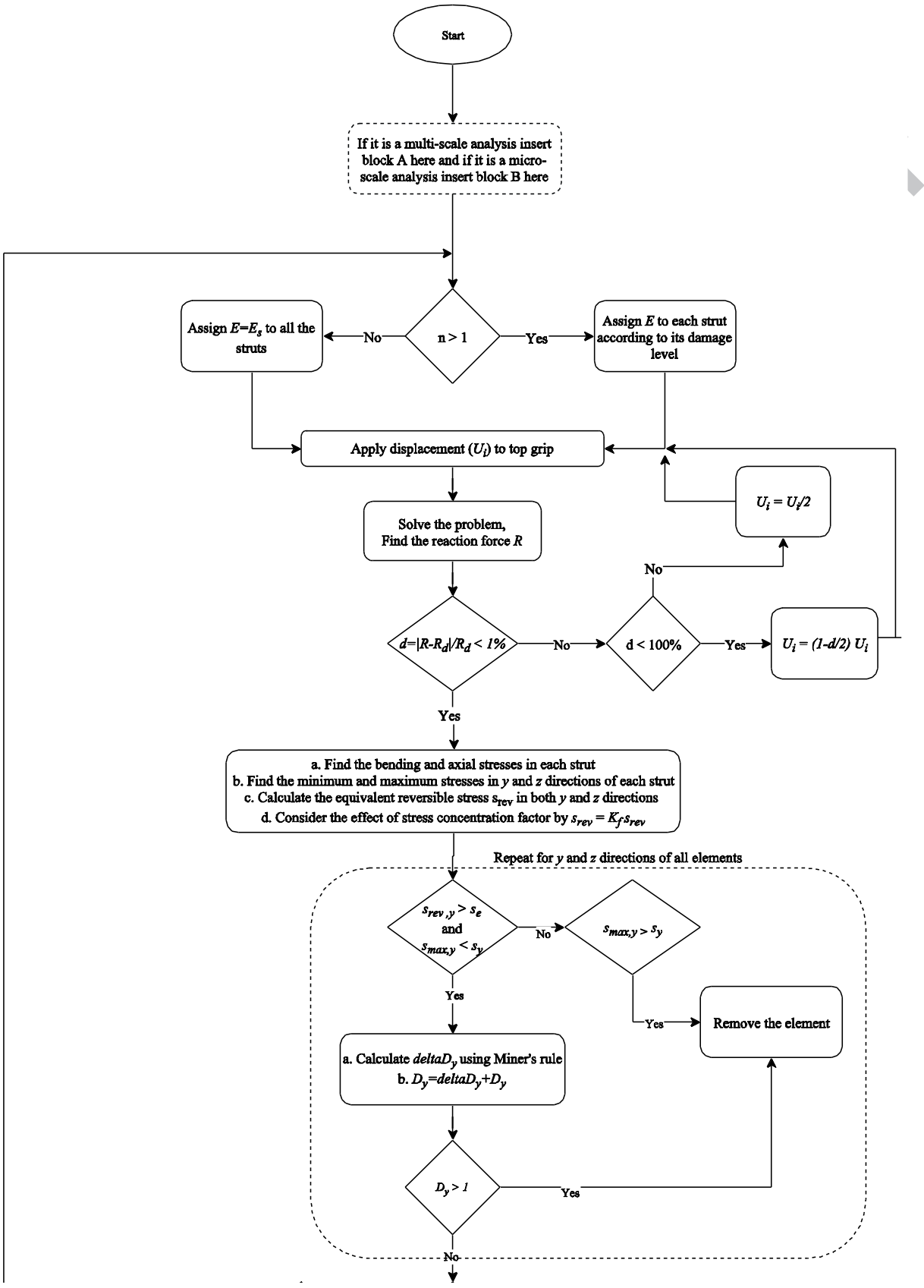

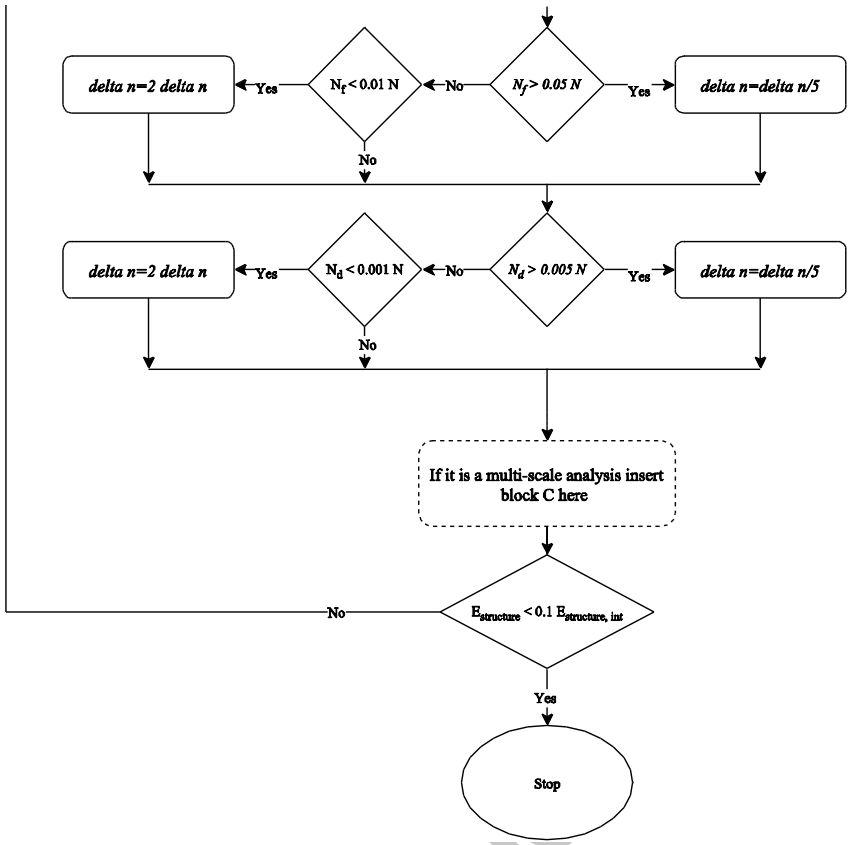

(a)

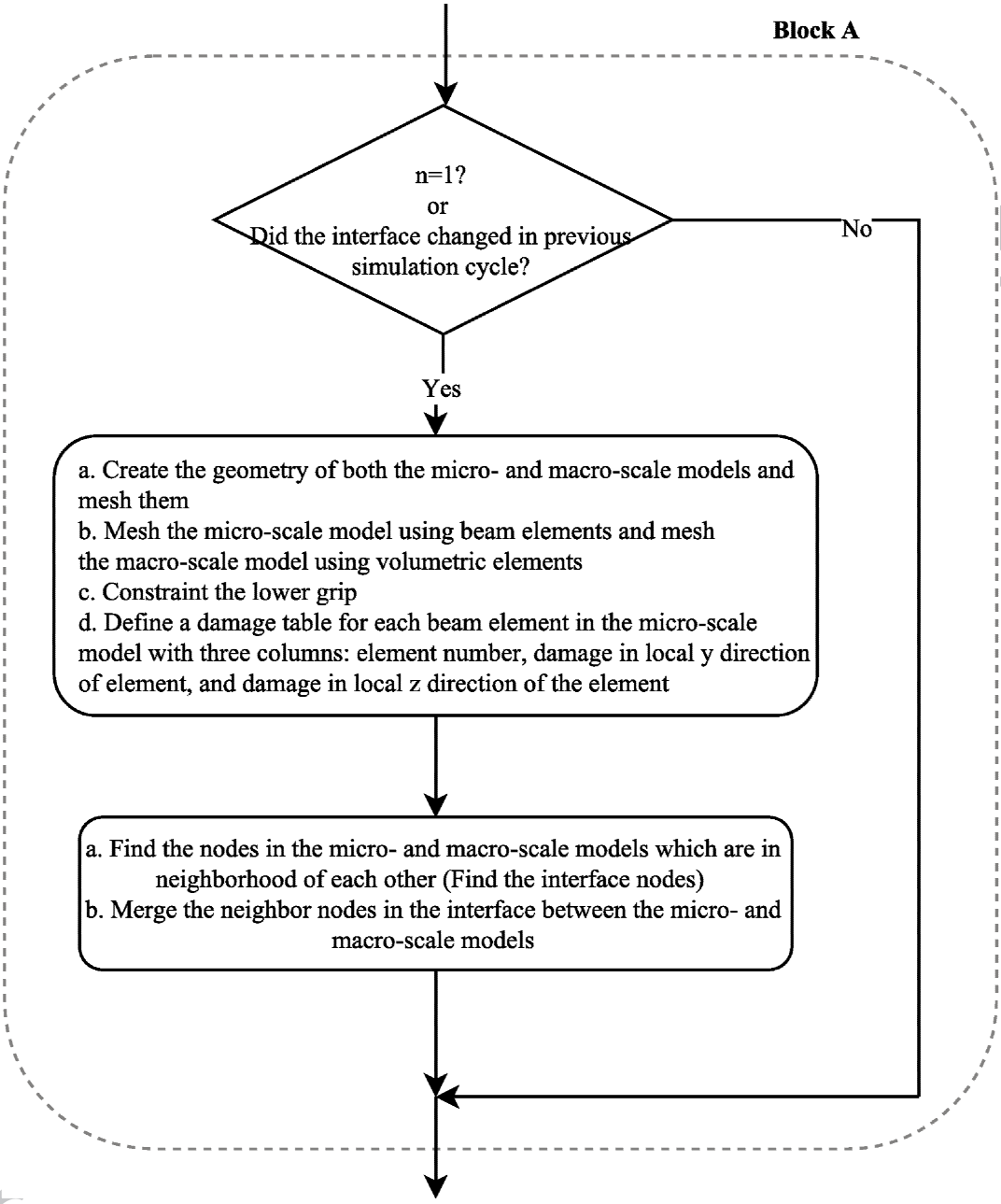

(b)

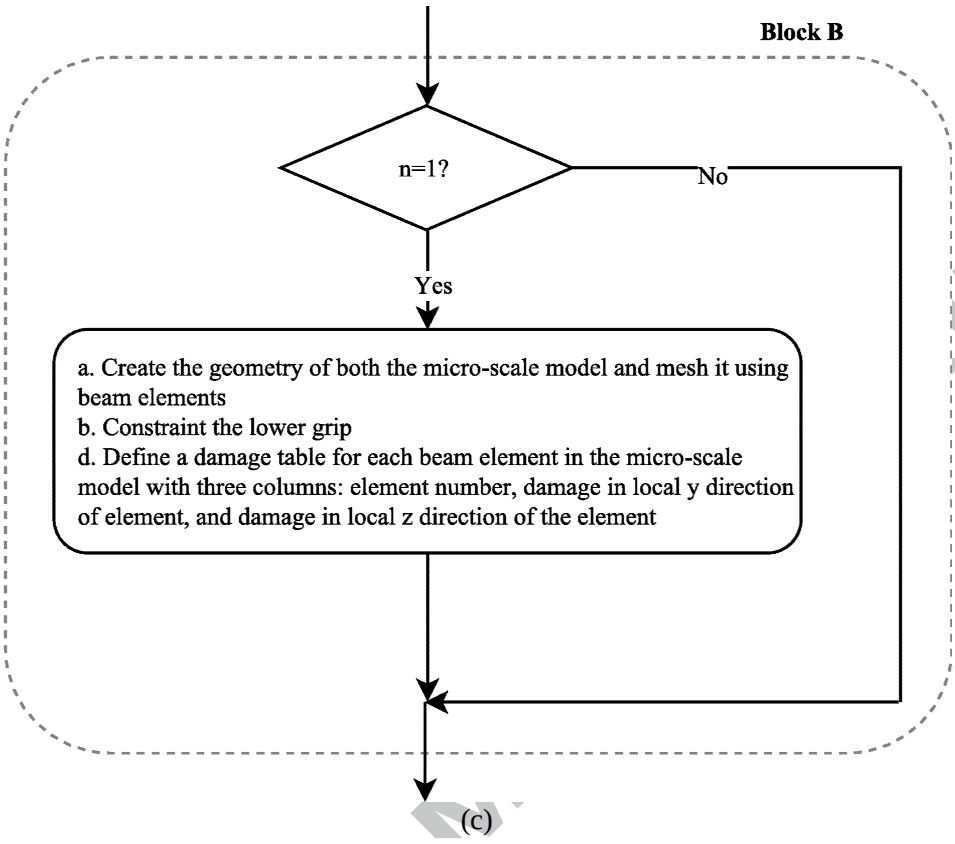

(c)

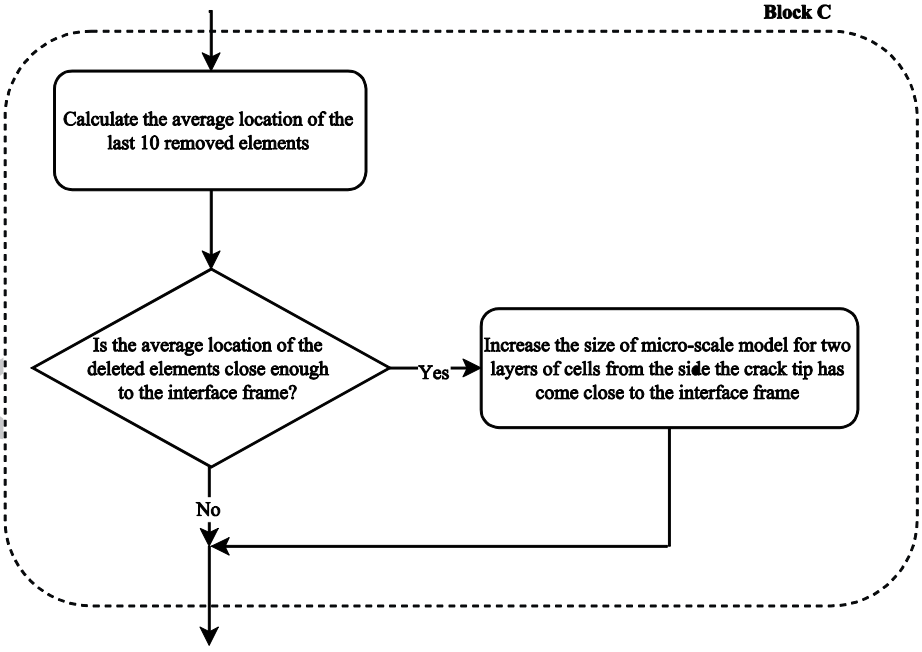

(d)

Figure 7- (a) The flowchart of the algorithm used for modeling damage propagation in the micro- or multi-scale models. The algorithms shown in flowcharts (b-d) are used as blocks in the main algorithm flowchart depending on the analysis type (micro-scale or multi-scale)

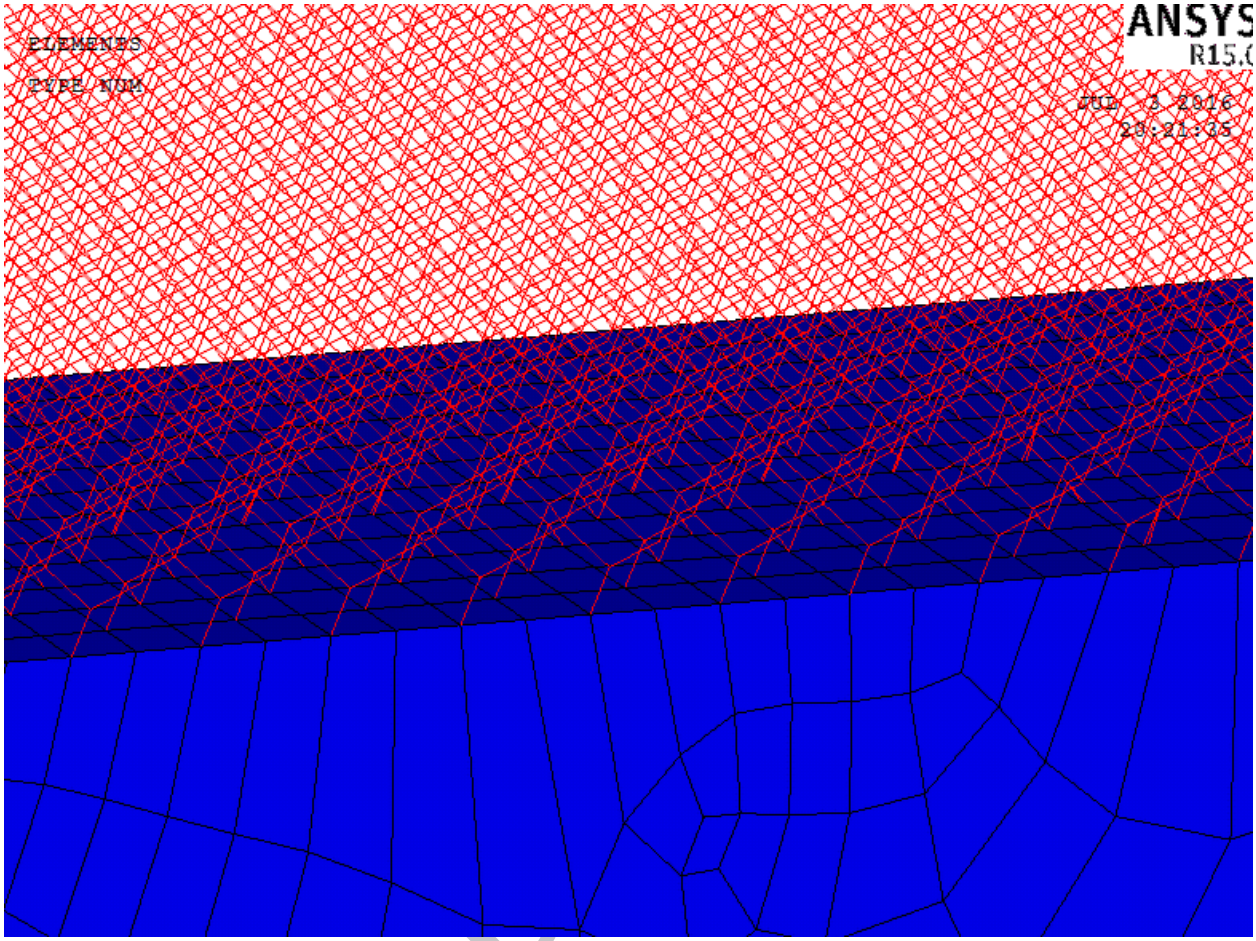

Figure 8- View of the interconnection area between the micro-scale and macro-scale parts in the multi-scale model. The macro-scale part was discretized in such a way that for each strut end located in the interface frame, there was a neighbor node in the macro-scale part.

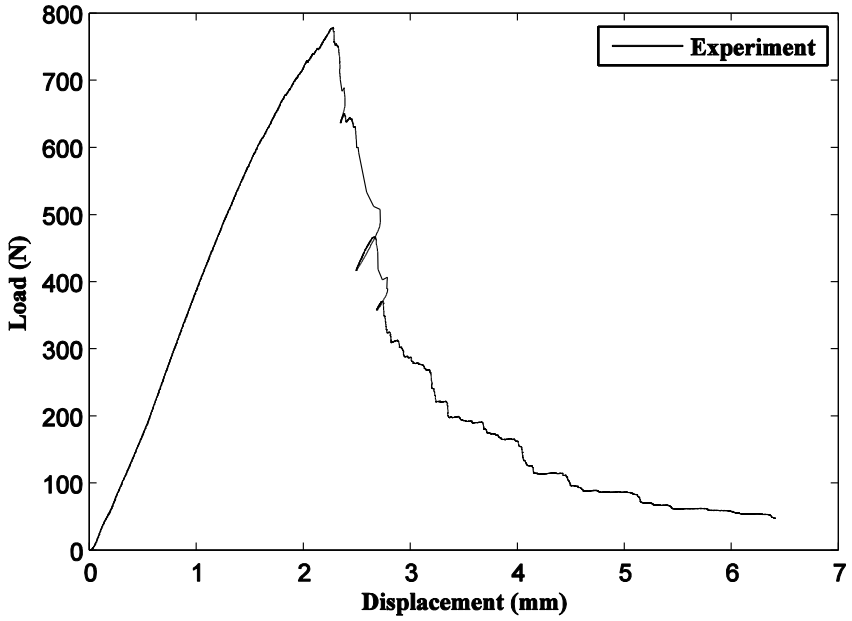

(a)

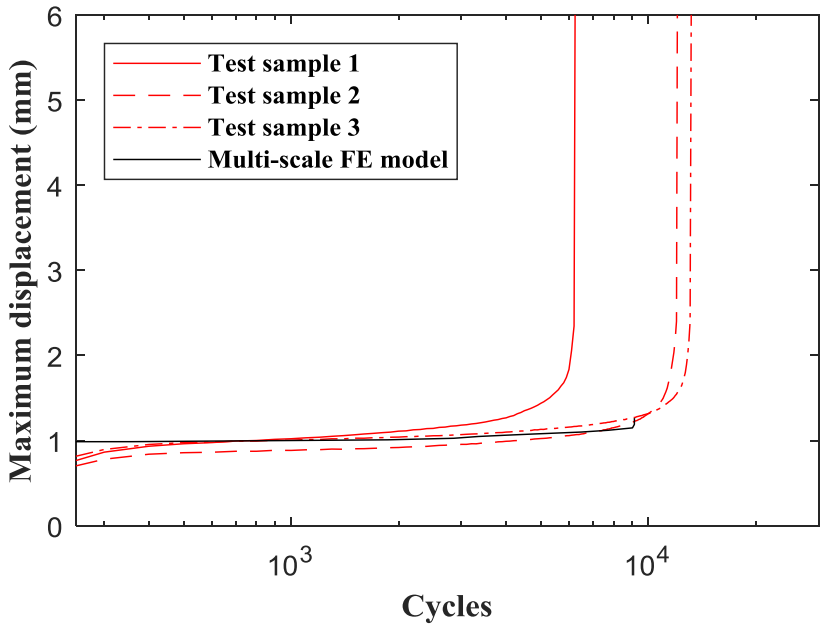

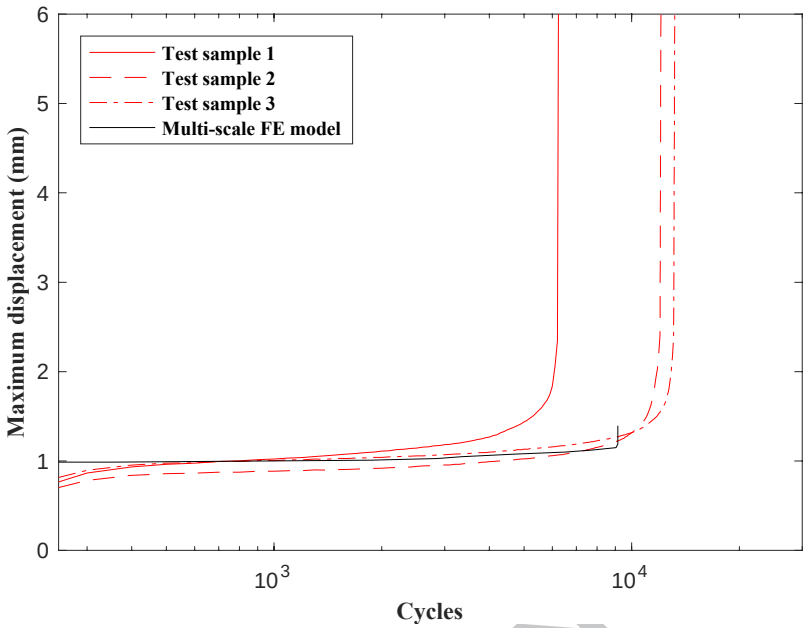

(b)

Figure 9- Comparison of experimental and numerical (a) load-displacement curves under static loading, and (b) displacement-cycle curves under fatigue loading.

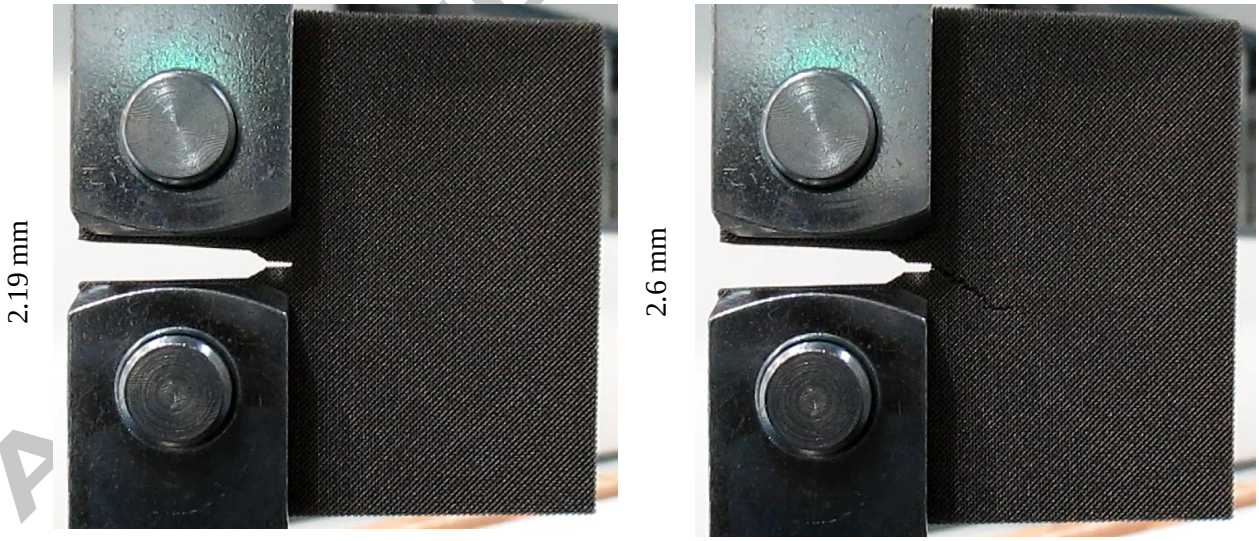

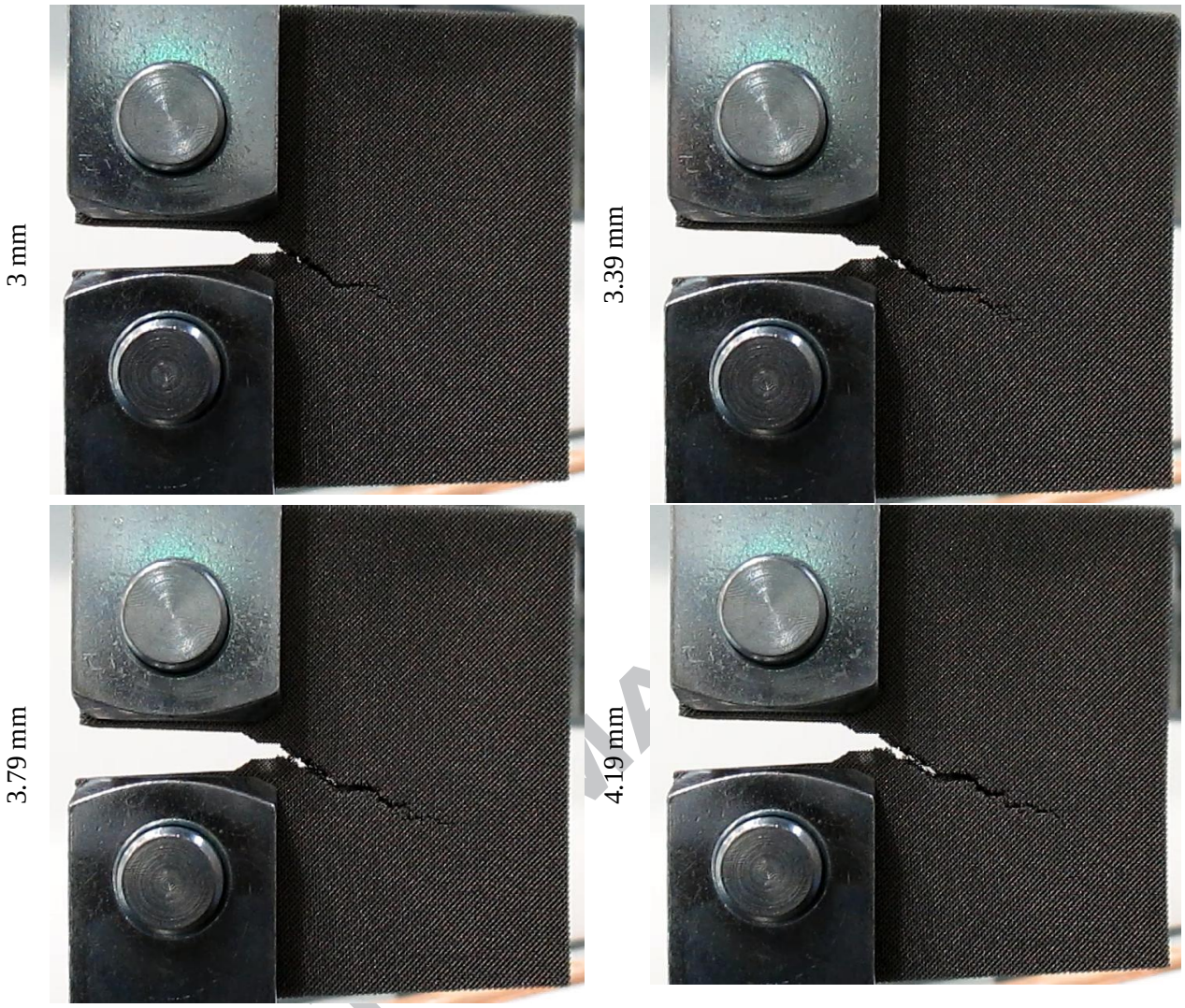

Figure 10- Sequence of damage propagation in the AM specimen (left) and in the corresponding multi-scale FE model under isostatic loading condition

Highlights

- A multi-scale computational approach was proposed to predict crack propagation
- The results of the multi-scale computational model matched the experimental results
- Considering plasticity in the material behavior of the parent material is important